# Fluid inclusions in magmatic ilmenite record degassing in basic magmas

Anthony Pochon, Daniel J. Kontak, Giada Iacono-Marziano, Eric Gloaguen, Johann Tuduri, Tom Chatelin, Jacques Précigout, Héctor Campos Rodríguez, Valentin Mollé, Blandine Gourcerol, et al.

communications earth & environment

Article

https://doi.org/10.1038/s43247-024-01788-8

# Fluid inclusions in magmatic ilmenite record degassing in basic magmas



Anthony Pochon [1,2] ✉, Daniel J. Kontak [3], Giada Iacono-Marziano[1], Eric Gloaguen [1,2,5], Johann Tuduri [1,2], Tom Chatelin[1], Jacques Précigout [1], Héctor Campos Rodríguez[1], Valentin Mollé[1], Blandine Gourcerol[2] & Loïs Monnier[4]

Magmatic volatile phases play a major role in igneous systems, but indirect sampling of the magmatic fluid, especially for basic magmas, remains challenging to document. Here, we report compelling evidence of primary fluid inclusions trapped within magmatic ilmenite from two different basic intrusive settings: Armorican Massif (France) and Central Iberian Zone (Spain). Fluid inclusions have a solute chemistry dominated by sodium, calcium, chlorine, sulfur and iron, with detectable contents of metals and metalloids and thus likely record the onset of late-stage magmatic volatile saturation in these basic magmas. Hence, we argue the presence of fluid inclusions in ilmenite may be a good indicator for magma degassing in these settings and importantly records the magmatic-hydrothermal transition. Additionally, this study suggests that the trapping of the magmatic volatile phase during ilmenite (and other opaque minerals) crystallization may be more common but at present an underappreciated phenomenon in basic igneous magmatic systems.

Fluids have played a major role in Earth evolution and its many geological processes. Since the pioneering work of Sorby[1], which provided petrographic evidence of fluid inclusions (FI) in a variety of mineral phases from diverse geological settings, these time capsules of paleo-fluids, the only direct samples of their former presence, have become fundamental tools for studying Earth processes. They have considerably contributed to the understanding of chemistry of the atmosphere and hydrosphere[2,3], sedimentary basin evolution[4], ore-forming processes[5], deep crustal fluid properties[6,7], and mantle volatiles[8]. Originally, FI studies were limited to minerals that transmitted visible light (400–700 nm) with quartz and carbonates among the most widely used. However, the advent of infrared (IR) cameras[9] revolutionized the application of FI studies by enabling their investigation in some opaque phases that transmit longer wavelengths of light from near infrared to beyond 2000 nm. This breakthrough expanded the scope of FI research to include a broader range of phases, such as oxides (e.g., hematite, wolframite), sulfides (e.g., pyrite, stibnite, Fe-rich sphalerite), and sulfosalts (e.g., tetrahedrite), as comprehensively summarized by Lüders[10].

Despite the progress made in applying the use of FI to numerous geological settings, debates continue about the role and significance of fluids in some geological processes. For instance, volatile saturation leading to magma degassing is critical for understanding magma ascent and eruption[11] (e.g., Cashman, 2004) and a prerequisite for many ore-forming processes[12–14] whereby fluid circulation associated with intermediate-to-felsic magmatism is considered fundamental to the origin of large hydrothermal metalliferous systems[5,15]. Conversely, the role of fluids in the formation of mafic-ultramafic intrusion-hosted magmatic sulfide and platinum-group element (PGE) deposits is still debated[14,16,17].

Although the former presence of volatiles dissolved in basic magmas is relatively well known due to studies of melt inclusions (MI)[18–21], sampling of these exsolved volatiles are rarely preserved in the plutonic settings of such magmas. However, some studies have inferred the former presence of such material preserved as FI in basic and mafic rocks[22–25]. These investigations were mainly focused on FI hosted in olivine, apatite, plagioclase or quartz in gabbroic rocks and related pegmatoids. In these latter rocks, the presence of early primary FI first indicates the early exsolution of $CO_2$-rich vapor from the melt which is consistent with solubility data and modeling of basaltic systems[26]. Subsequently, during progressive crystallization, the later-stage residual evolved melts attained volatile saturation as reflected by the entrapment of either immiscible[22–24] (i.e., $H_2O$-$CO_2$-NaCl ± Fe-rich brines and $H_2O$-$CO_2$-rich vapors) or homogeneous[22,23,27] volatile phases. Two main processes have been suggested to explain the generation of brine variations in gabbroic rocks. The first implies exsolution of magmatic fluids under supercritical conditions with condensation of immiscible droplets of brine in a vapor phase[24,28–31]. In contrast, the second involves direct exsolution of highly-saline magmatic fluids from residual, evolved, late-stage

[1]ISTO, UMR7327, Université d'Orléans, CNRS, BRGM, F-45071 Orléans, France. [2]BRGM, F-45060 Orléans, France. [3]Harquail School of Earth Sciences, Laurentian University, Sudbury, Ontario, P3C 2E6, Canada. [4]GET, CNRS/IRD/UPS/CNES, Université de Toulouse, 31400 Toulouse, France. [5]Deceased: Eric Gloaguen ✉e-mail: a.pochon@brgm.fr

melts in the absence of a discrete vapor phase[22,23,27,29,32,33]. These gabbroic-hosted FI of magmatic origin may also contain noticeable amounts of Ca, S, and metals[25] (e.g., Cu, Zn and Pb). However, the ability to study magmatic FI in basic rocks is not always possible as phases commonly hosting FI are either often lacking (e.g., quartz or olivine) or commonly modified by later fluids (e.g., apatite, plagioclase).

In order to document saturation of a magmatic volatile phase (MVP) in two separate basic (mafic) plutonic settings, we have applied a wide range of analytical methods to test for the preservation of such fluids in ilmenite, as it is a common late-stage magmatic phase in these systems. Here we present compelling evidence arguing for the entrapment of primary FI in magmatic ilmenite during the latter stages of crystallization of the residual melts. Additionally, we also document qualitatively the composition of these trapped fluids, the results of which are consistent with that known and expected for magmatic fluids associated with basic magmas. As ilmenite is common in many reduced, basic-to-intermediate magmas, we propose therefore that ilmenite might be considered as a potential host for FI containing magmatic fluids in such rocks. Therefore, researchers seeking evidence for the former existence of such fluids should consider examining this mineral phase, especially when other hosts for FI are not preserved or subsequently modified by subsolidus processes.

## Geological background

The samples used in the study originate from two different basic intrusions: the Saint-Jean-du-Doigt (SJD) intrusion (Armorican Massif, France) and the La Codosera (CS) syncline basic sills (Central Iberian Zone, Spain, Supplementary Fig. 1). The SJD intrusion is a shallow-level, layered basic-silicic intrusive body emplaced at ca. 347 Ma[34] within Paleoproterozoic to Carboniferous host rocks. The pluton is mainly composed of underplated subhorizontal gabbroic sills with some sub-parallel felsic layers, subordinate crosscutting dolerite dykes and genetically-related basic amphibole-bearing pegmatoids[35]. It is exposed along a continuous west-to-east cross-section commencing with the lower part of the intrusion and finishing in its roof zone[34,36]. The mineralogical composition of the sampled rocks is presented in Supplementary Table 1. It has been demonstrated that an increase of high-temperature alteration occurs eastwards towards the intrusion roof, as evidenced from the complete saussuritization of calcic plagioclase, pervasive replacement of clinopyroxene and primary amphibole by actinolite, and the breakdown of ilmenite to titanite and rutile[36]. This progressive alteration has been interpreted to result from the interaction of almost solidified gabbro with magmatic fluids posited to have exsolved during its late magmatic stage and thus reflecting the magmatic-hydrothermal transition within the SJD basic intrusive body[36].

The basic intrusions from CS consist of a major swarm of sills up to 400 m thickness hosted in Carboniferous slates. These sills are attributed to a single-pulse of tholeiitic basic magma emplaced at 354 ± 5 Ma[37]. The sills are mainly composed of a floor and a roof sequence of gabbroic and doleritic rocks with interleaved pegmatitic units that are well described by López-Moro et al. [38,39]. At the base, a pristine mineralogy is preserved in a fine-grained dolerite whereas the central part is coarse-grained gabbro. The intensely altered (e.g., amphibole) roof zone consists of fine-grained dolerite (mineralogical composition in Supplementary Table 1) with abundant pegmatite lenses.

## Results

### Textural description of ilmenite

Ilmenite crystals are subhedral to anhedral in the gabbroic and doleritic facies of both basic systems. They are mostly intergranular and occur along grain boundaries between plagioclase and amphibole, or clinopyroxene, or between primary amphibole and later low-temperature amphibole. Ilmenite is considered therefore to represent a primary, late-stage magmatic phase[36,39]. For SJD samples, ilmenite has a grain size ranging between 100 and 2000 μm with smaller grains in the upper part and larger ones in the central part of the complex. It is texturally homogeneous in backscattered electron (BSE) images (Fig. 1A–C) and lacks hematite exsolution textures. For CS samples, it is again mostly homogeneous in BSE images with similar grain size, but some hematite exsolution textures are observed (Fig. 1D). Ilmenite from SJD is chemically uniform and near end-member composition, whereas for CS samples, its chemistry deviates from that of the end-member and falls along the ilmenite-hematite solid solution (Fig. 2, Supplementary Table 2). These data indicate that slightly more oxidizing conditions prevailed during crystallization of ilmenite from CS versus SJD.

Ilmenites from the SJD intrusion (central and upper part) and the CS basic sills (upper part) are characterized on their exposed surfaces by a high abundance of well-distributed voids with sizes ranging between 0.5 and 7 μm, most of them being lower than 2 μm (Fig. 1B–J); in contrast ilmenite from the lower part of SJD intrusion is noted to lack observable voids (Fig. 1A). The outlines of these voids vary from spherical, equant to multi-faceted negative-crystal shapes (Fig. 1I, J). Such negative shapes are commonly observed in FI-bearing transparent phases (e.g., quartz or carbonate) examined in both transmitted (TL) and reflected (RL) light modes, as well as BSE imaging[40–42]. These voids are thus posited to correspond to breached or opened FI. As the 2D polished cuts of ilmenite studied are presumed to reflect ilmenite grains with random orientations, it is therefore inferred that the FI locally account for up to 15% of the total crystal volume. The opened FI are mostly homogeneous in their distribution throughout the ilmenite grains, but also define sub-parallel trails (Fig. 1C, J) or are concentrically distributed about silicate-rich inclusions (Fig. 1H). In rare cases, opened FI are heterogeneously distributed and may include solids such as gold, barite, and Pt- and Sr-bearing phases (Supplementary Fig. 2).

In most ilmenite crystals, textural observations highlight that rims are devoid of FI (Fig. 1C), and that crack-like channels and irregular-shaped areas barren of FI may also traverse the otherwise FI-rich ilmenite. These latter areas are often spatially linked to titanite, or contain irregular patches of titanite ± rutile (Fig. 1E–G). Such ilmenite likely records variable amounts of subsolidus replacement post its crystallization (Fig. 1E, F) with some grains replaced via fluid interaction by up to 80% by titanite and/or rutile in the most altered samples (Supplementary Fig. 2). Titanite and rutile are commonly present as reaction rims and also lining thin fractures and cavities in both settings. Additionally, contacts between ilmenite and its alteration products are sharp and irregular.

Electron backscatter diffraction (EBSD) maps reveal that the most misoriented parts of ilmenite grains follow what appear to be fluid-like pathways coincident with fractures and areas barren of FI (Fig. 3A–C). These FI-free cracks are often filled with titanite ± rutile (Fig. 1G). In contrast, the EBSD patterns for FI-rich areas are relatively uniform and closely resemble the patterns for FI-free ilmenite from the lower part of the SJD intrusion (Supplementary Fig. 3). Chemical maps (Fig. 3D, Supplementary Fig. 3) show that FI-rich and FI-free areas of ilmenite have a similar chemistry, the only subtle differences being due to the presence of FI.

### Insight into magmatic fluid chemistry

The chemistry of trapped FI was determined via two indirect methods: (i) LA ICP-MS analyses of distinct FI-free and FI-bearing areas of ilmenite; and (ii) coupled SEM-EDS, EPMA, and LA ICP-MS analyses of evaporate mounds. The LA ICP-MS analyses of ilmenite (Fig. 4A) yield concentrations with a similar order of magnitude for most compatible trace elements[43,44] (i.e., V, Nb, Ta, Co, Zn, Ni) in both settings (SJD and CS) and both distinct FI-free and FI-bearing areas. Except for Cu concentration in both settings and W concentration in the CS setting that show the same order of magnitude for FI-free and FI-bearing areas, most incompatible trace elements[43–46] (i.e., Sn, Mo, Sb, W, Pb) are enriched in FI-bearing areas. This observation is corroborated by LA ICP-MS traverses (Fig. 4B) which highlight no sharp differences for Ni and Cu, but clear enrichment in Sb and Mo when crosscutting FI-bearing areas. Again, when LA ICP-MS traverses (Fig. 4C) crosscut FI-free ilmenite from the lower part of the SJD intrusion, Sb and Mo are below the detection limit. These latter observations suggest the incompatible elements are most likely concentrated in FI. The Sb, Mo, Sn, W (for SJD only), and Pb contents generally show larger variability in FI-bearing areas and also have different degrees of enrichment between the two

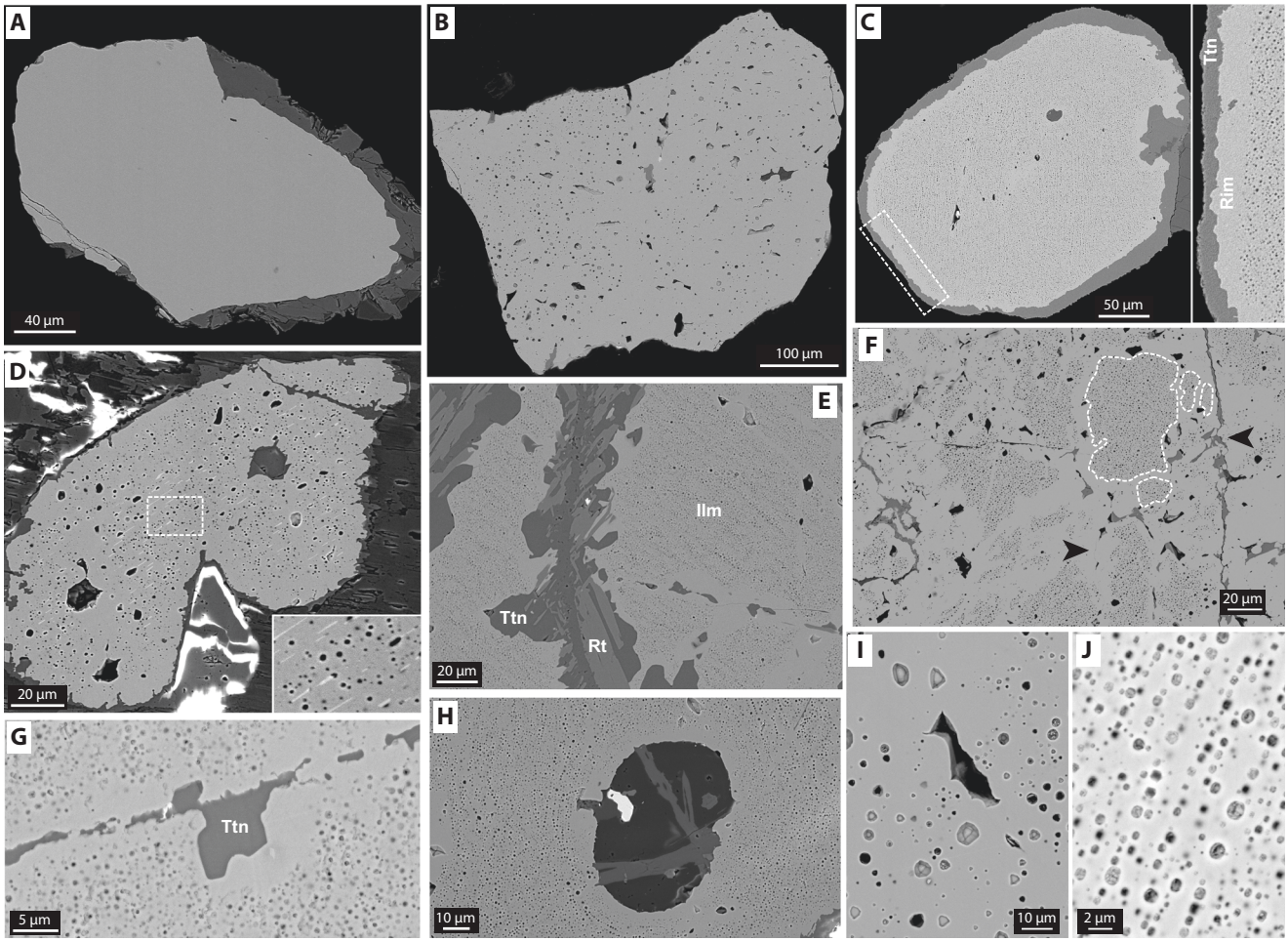


**Fig. 1 | Representative back-scattered electron (BSE) images of textural and petrographic features of ilmenite from both settings.** Ilmenite from the lower (**A**), central (**B**) and upper (**C**) parts of the Saint-Jean-du-Doigt (SJD) intrusion. The inset in (**C**) shows the crystal core is full of FI, whereas the rim is FI depleted and replaced by titanite (Ttn). **D** Ilmenite from La Codosera syncline (CS) showing the presence of FI and hematite exsolution lamellae (see the inset). **E** Ilmenite (Ilm) from SJD showing alteration along fractures or fluid pathways with formation of secondary titanite (Ttn) and rutile (Rt). **F** Ilmenite from CS with abundant FI and exhibiting the same secondary texture seen in the SJD samples: cracks are sometimes lined by titanite, and have halos lacking FI (black arrows) which form isolated patches of FI-rich areas (white dashed lines). **G** Sample from SJD showing a fracture lined by secondary titanite (Ttn) with a halo lacking FI. **H** Ilmenite from CS displaying the radial distribution of FI around silicate-rich inclusions. **I, J** Sample from SJD showing opened FI with negative shapes of the ilmenite host (**I**) that are often uniformly oriented (**J**).

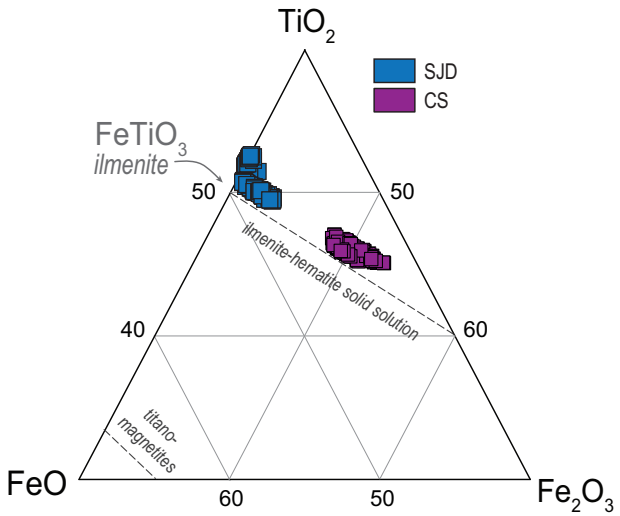


**Fig. 2 | Major element composition of ilmenite.** Ternary plot of the FeO-$Fe_2O_3$-$TiO_2$ system showing the hematite-ilmenite solid solution[86] and data for Saint-Jean-du-Doigt (SJD) and La Codosera syncline (CS) samples. Data for SJD is from Pochon et al[36].

settings likely reflects distinct fluid chemistries, although heterogeneities related to the FI which are located at different depths below the surface and analytical uncertainties are difficult to assess.

The mounds generated by induced decrepitation of FI (Fig. 5) vary from small isolated features (Fig. 5A, E, F–H) to trails (Fig. 5B–E) in addition to abundant debris that represents splattering of precipitates and projection of fragmented mineral host away from the core areas of the mounds; all these features have shapes from irregular to cubic which are typical mound characteristics[42]. High-resolution X-ray maps show that the major element solute chemistry of the mounds is dominated by Na and Ca, with Fe, as cations, and by Cl and S, as anions (Fig. 6A, B, Supplementary Fig. 4), as is also confirmed by the LA ICP-MS traverses (Fig. 6C, D, Supplementary Fig. 5). The aqueous and non-aqueous volatile or gas content (e.g., $H_2O$, $CO_2$ or $CH_4$) cannot be determined with this protocol. The LA ICP-MS traverses also indicate increasing contents of the incompatible trace element (e.g., Sr, As, Sb, Cu) in mounds from FI-rich areas of ilmenite compared to FI-free areas (Fig. 4).

## Discussion

We observed that crystallized ilmenite of magmatic origin from two different settings contain voids that are strikingly similar to FI regularly seen in both transparent and opaque phases via TL and IR observations. As far as we

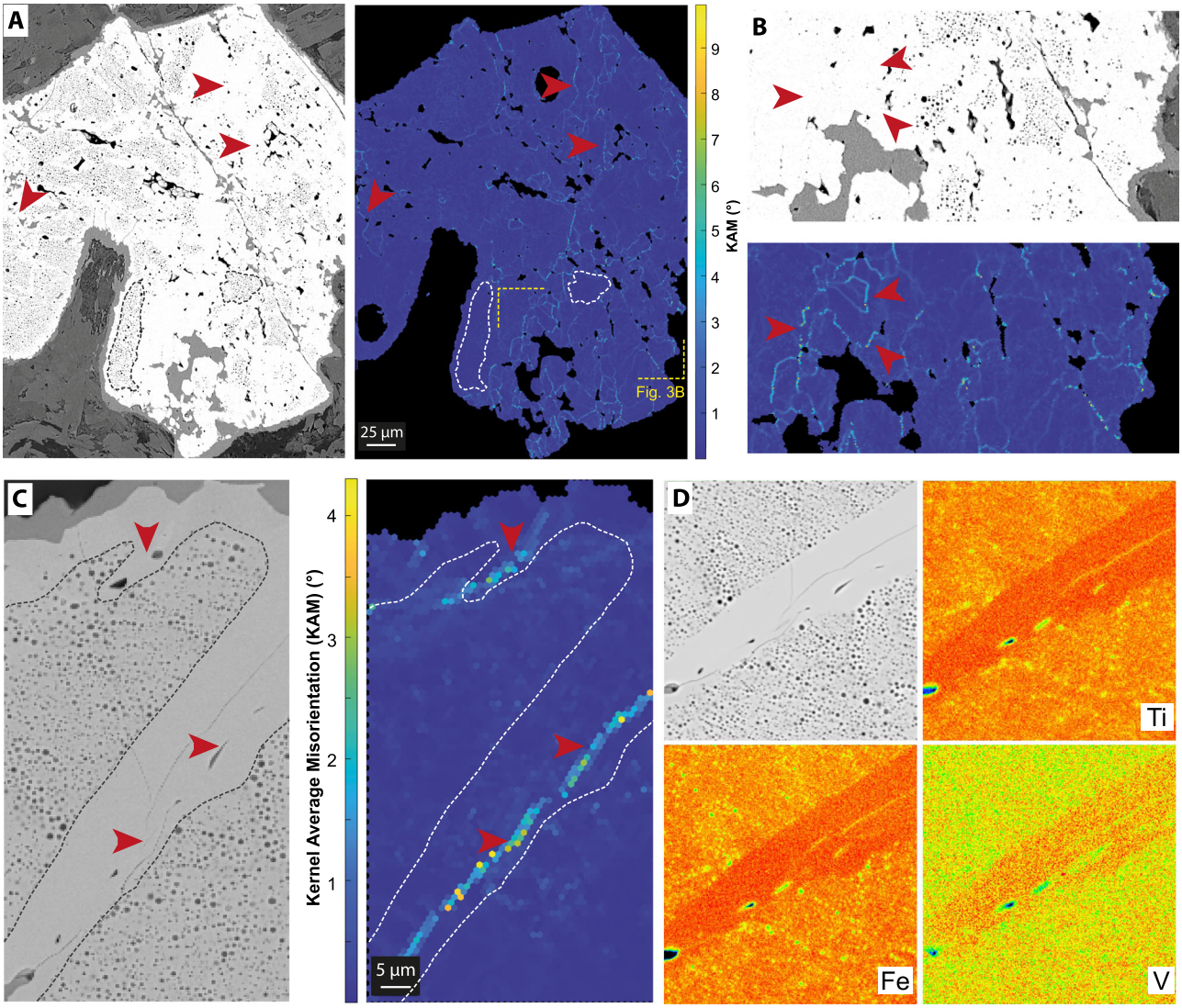


**Fig. 3 | Representative electron backscatter diffraction (EBSD) and high-resolution X-rays maps of ilmenite from both Saint-Jean-du-Doigt (SJD) and La Codosera syncline (CS). A**, **B** Back-scattered electron (BSE) images of ilmenite with matching EBSD maps representing the Kernel Average Misorientation (KAM). Sample is from the upper part of the CS intrusion. White dashed line and red arrows, respectively, highlight FI-rich areas and fractures. Yellow dashed line inset corresponds to the area observed in (**B**). **C** BSE image of ilmenite with matching EBSD map representing the KAM. Sample is from the upper part of SJD intrusion. Dashed line and red arrows, respectively, highlight FI-rich areas and fractures. **D** High-resolution X-ray maps for Ti, V, and Fe of the same ilmenite grain than from (**C**) with a FI-depleted zone developed around a central fracture.

know, this is the first report of inferred FI in magmatic ilmenite. We therefore reiterate the evidence which shows that these are indeed fluid inclusions[40]: (i) their size and shape are similar to typical FI; (ii) many are negative shaped as is common for FI; (iii) they are mostly homogenously distributed throughout the host in both two- and three dimensions (Supplementary Fig. 6); and (iv) heating ilmenite up to 600 °C generated Na-Ca salt mounds identical in form and chemistry (i.e., Na-Ca-Cl-S) to those formed from FI hosted in both transparent and opaque phases[42].

EBSD maps indicate that FI-free areas, often associated with titanite ± rutile, are secondary in origin compared to FI-bearing areas. Thus, whereas FI-bearing areas in ilmenite from both intrusions are posited to represent relics of primary magmatic ilmenite hosting FI, the FI-barren areas are interpreted as post-magmatic in origin and attributed to subsolidus reaction of the host ilmenite with fracture-controlled incursion of a Ca-bearing hydrous phase. The irregular and sharp contacts between ilmenite and titanite ± rutile, the preserved shapes of ilmenite and titanite ± rutile -bearing cracks strongly suggests that the ilmenite breakdown occurred via interface-coupled dissolution-precipitation process (ICDP)[47–49], thus post-dating FI entrapment. All these observations suggest therefore that FI in the magmatic ilmenite are primary and thus likely represent entrapment of an exsolved MVP. Alternatively, the trapped FI might be considered as an ICDP-related porosity[50] and hence of secondary origin, but this would not corroborate the textural observations and EBSD data presented above. Most important in this regard is that in ICDP the porosity generally characterizes the product phase which thereby implies the ilmenite to be of secondary origin, which is evidently not the case. Furthermore, no relic-clear areas were noted in any studied ilmenite (i.e., about 400 grains examined) and it is very unlikely that such secondary porosity was only filled by fluids with no mineral phase. We conclude therefore that the most reasonable interpretation of the noted features is that they are primary FI trapped during growth of the ilmenite. Their negative shapes are however a secondary feature, as in all FI, and due to the equilibration of the FIs during cooling via dissolution-precipitation processes to minimize surface free energy[40,41]. In any case, the occurrence of primary FI in magmatic ilmenite demands the presence of a fluid phase that we interpret as an exsolved MVP generated during the latter stage of magma crystallization at the magmatic-hydrothermal transition (Fig. 7) related to second boiling[51]. Importantly,

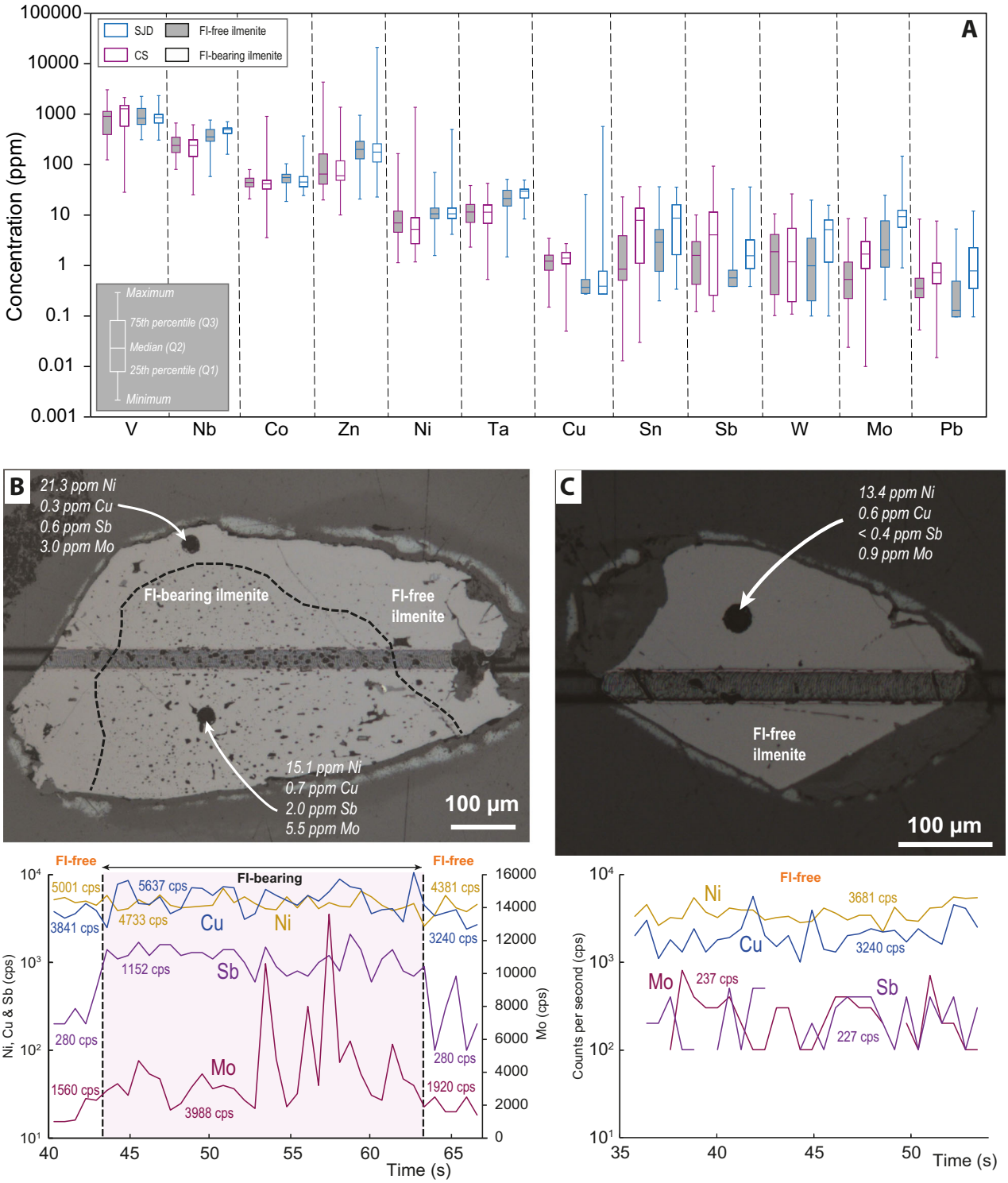


**Fig. 4 | Trace element composition of ilmenite. A** Box plots for trace element contents in FI-bearing and FI-free ilmenite from Saint-Jean-du-Doigt (SJD) and La Codosera syncline (CS) samples. LA ICP-MS traverses of (**B**) ilmenite from the central part of SJD intrusion with FI-free and FI-bearing domains and (**C**) FI-free ilmenite from the lower part of the SJD intrusion. Spot analyses data for SJD are from Pochon et al.[36].

we note, however, that MI have not been identified in any ilmenite from either setting, which does not necessarily infer that they were not trapped but may instead reflect the challenges of identifying them. Of note however is that if MI were exposed at the ilmenite surface, it would be difficult to distinguish if these originated as silicate embayments or crystal intergrowths versus crystallized MI[40,52,53]. As an example of the latter, we noted the presence of the silicate-rich inclusion in Fig. 1H.

Although there is petrological evidence for a hydrous component in the melt, as indicated by the presence of amphibole and biotite, only cryptic evidence for the former presence of an aqueous fluid phase is generally preserved in plutonic rocks[21], especially because of the inherently slow post-solidus modification that affects plutons compared to their petrogenetically equivalent chilled volcanic rocks. However, the presence of posited primary FI in ilmenite makes this mineral an ideal candidate to trap and preserve the

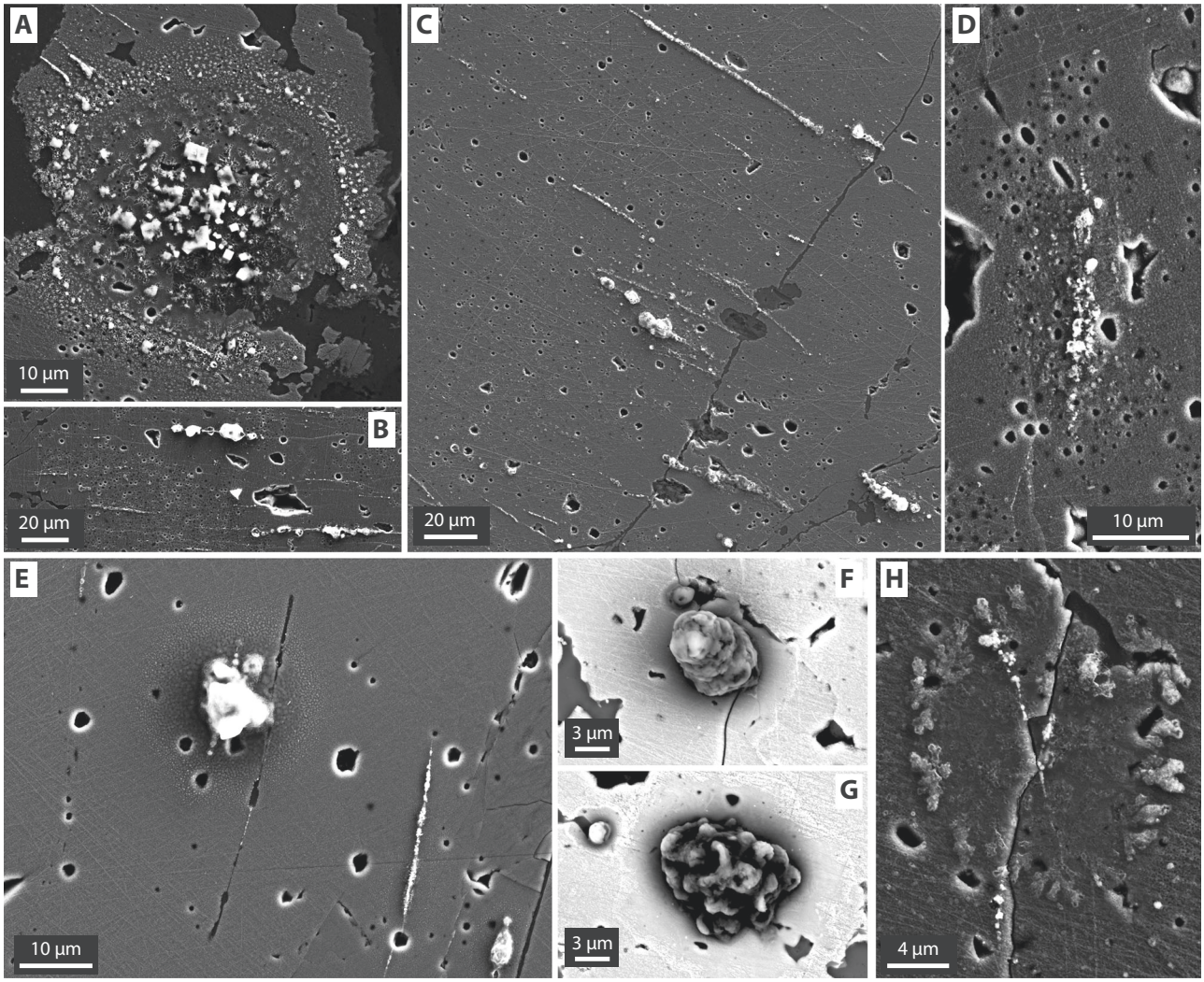


**Fig. 5 | Examples of Na-Ca-rich decrepitate mounds from Saint-Jean-du-Doigt (SJD) and La Codosera syncline (CS). A** Secondary electron (SE) image of a composite circular evaporate mound from CS; note the cubic habit of the material in the central part and annular array of debris. **B**–**E** SE images of decrepitate mounds that form trails and clusters that reflect the presence of FI-rich areas in the subsurface of ilmenite from SJD (**C**, **E**) and CS (**B**, **D**) settings. The trails are the result the fluid migrating up along fractures which were preexisting or generated by the decrepitation. **F**, **G** Close-up back-scattered electron (BSE) images of singular evaporate mounds from CS samples. **H** SE image of circular and partly dendritic mound from CS sample.

MVP as primary FI in basic plutonic rocks. This can offer new perspectives where conventional convincing indicators for the generation of MVP commonly observed in more intermediate-to-felsic magmas, such as comb-layered quartz, miarolitic cavities, or pegmatites, are lacking or not preserved[54,55]. Thus, where such FI are present their chemistry (e.g., analysis of evaporate mounds) provides the means to access the metal abundances in magmatic fluids exsolved during the last crystallization stages of basic magmas. The solute composition (i.e., Na-Ca-Cl-S-Fe) and presence of metals and metalloids are indeed consistent with those noted to be enriched in arc-related volcanic gases from basic magmas[56,57] (i.e., Cu, Sn, Mo, Sb, W, and Pb). Although we were unable to measure the aqueous and non-aqueous volatile component (or gas), we infer the MVP to be $H_2O$-dominated as magmatic amphibole is present and ilmenite is a late-magmatic phase. Indeed, experimentally-based solubility models and studies of volatile contents in MI show that the exsolved volatile phase coexisting with basic magmas is $CO_2$-rich during early crystallization stages, and increasingly $H_2O$-rich with subsequent crystallization[21]. Both first boiling (due to magma decompression) and second boiling (due to magma crystallization) lead to an increase in $H_2O$ proportion in the exsolved volatile phase. This is mainly due to the fact that $H_2O$ solubility is higher that $CO_2$ solubility in basic magmas, as it is for all silicate magmas[58], at crustal pressures, and, to a lesser extent, to the different relationships between pressure and solubility, i.e., linear for $CO_2$ and square root for $H_2O$[59].

As evidenced by the presence of primary FI, the late residual melts of these two basic magmas were volatile saturated, but the extreme abundance of trapped fluid (i.e., up to 15 % of the crystal volume noted above) in ilmenite raises questions, especially about processes leading to fluid entrapment. Three mechanisms might account for the generation of FI are considered below, although we do not consider the first two applicable to the present study for reasons discussed. The first is that the FI may have originated from exsolution of dissolved water hosted in the ilmenite crystal lattice. This implies the FI were released directly from the host after it formed, thus analogous to that suggested for origin of FI in some metamorphic host phases such as quartz[60], kyanite[61] or omphacite in UHP eclogite[62]. Implicit therefore is that ilmenite incorporated some amount of a hydrous species, as suggested for some nominally anhydrous minerals such as pyroxenes or rutile[63]. Several factors argue against this however. The lack of any data supporting incorporation of some amount of hydrous species into the ilmenite structure. Furthermore, even if this occurred the likely trace amount of water would be insufficient to generate the abundance of the FI observed which we estimated at up to 15% of the ilmenite volume. Lastly, such FI would likely not contain the Na, Cl or S documented in this study as

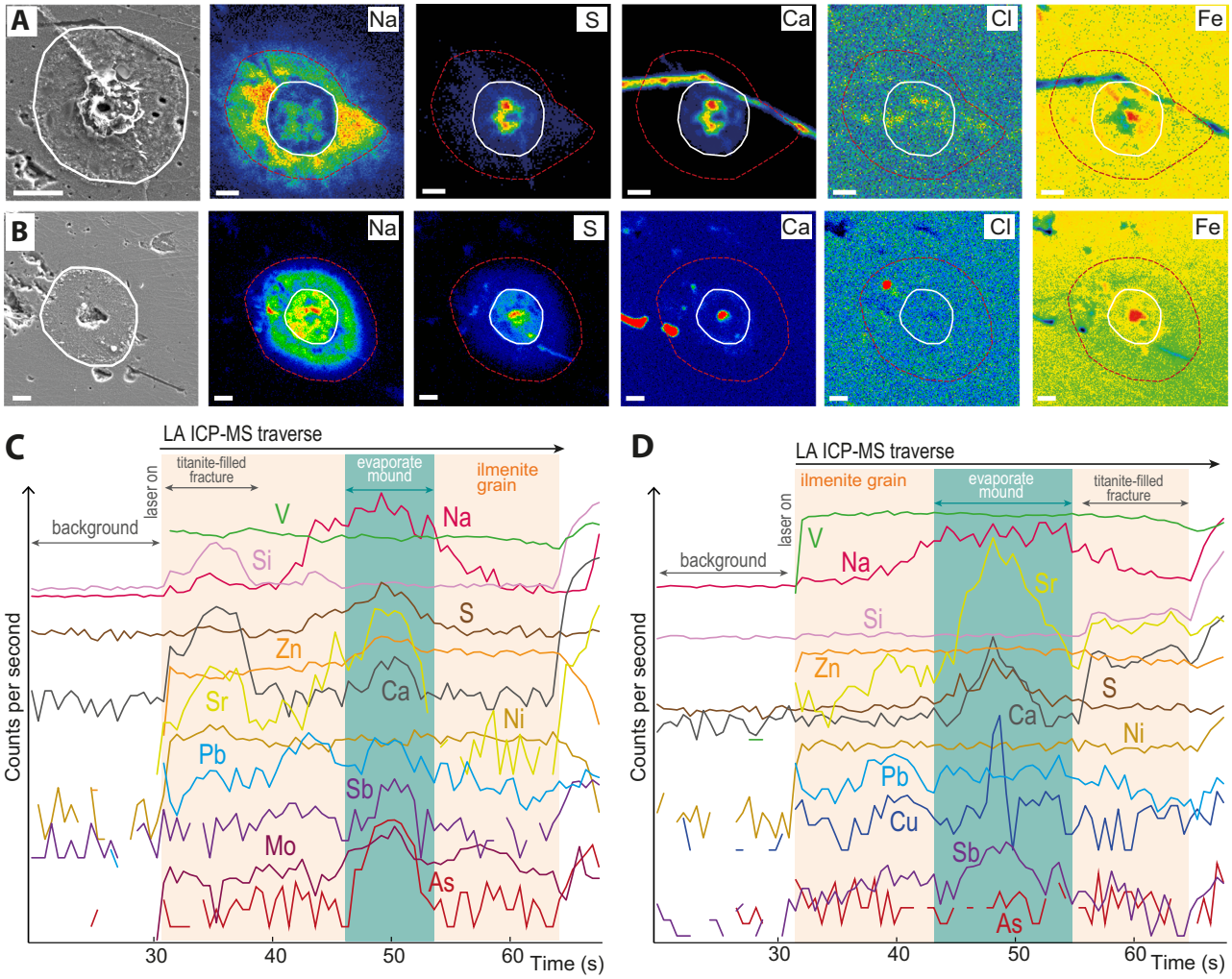


**Fig. 6 | Representative chemical maps and time-resolved LA ICP-MS signals of circular evaporate mounds from Saint-Jean-du-Doigt. A**, **B** Chemical maps for representative circular evaporate mounds obtained via electron probe micro-analysis (EPMA). White line circumscribes the mound, while the red-dashed line circumscribes the halo around the mound. White bar in images is 10 µm. **C**, **D** Time-resolved traverses of LA ICP-MS analysis of decrepitated mounds from the same ilmenite grains in (**A**) and (**B**), respectively. The curves have been offset vertically for clarity and truncated curves represent zero counts.

these elements would also have to be in the ilmenite crystal lattice and also be exsolved synchronously with the hydrous species. The second mechanism is that ilmenite directly crystallized from the MVP, thus be considered as a hydrothermal phase. However, this is unlikely as the rare cases where ilmenite is interpreted as hydrothermal is reported to be Mn- and/or Zn-rich[64,65], which is clearly not the case noted in this study.

We thus propose a third mechanism which might account for the generation of the noted FI hosted by ilmenite. As we have interpreted the FI to represent sampling of an exsolved $H_2O$-dominated MVP related to second boiling, it implies that residual melt will become $H_2O$-saturated at the very end of crystallization (i.e., 95 % crystallization[51]). From this stage, the documented abundant entrapment of FI by ilmenite could result from the transient trapping of exsolved bubbles in the crystal mush followed by the near-simultaneous nucleation of both ilmenite and bubbles. Thus at the time of ilmenite crystallization a component of the exsolved MVP must have been present as bubbles, at least transiently, in the residual melt of the mush, otherwise a connectivity of the MVP would have formed fluid-like channels which would have caused outgassing of the volatiles[66,67]. Therefore, it is possible the ilmenite may have acted as a preferential site of bubble nucleation, as is generally observed for Fe-Ti oxides[68–70]. However, both natural analogues[71] and experimental evidence[72] of bubble nucleation show that Fe-Ti oxides are generally smaller than coexisting bubbles which are in fact sometimes trapped inside them, which is contrary to our observations. Ilmenite larger than the trapped bubbles could be explained if we consider a crystallization rate fast enough to prevent bubble coalescence and growth. A $CO_2$-bearing melt may be also envisaged, as low-$CO_2$ diffusivity delays bubble growth and thus promotes almost continuous bubble nucleation which would result in a high density of small bubbles[73]. However, if the exsolved MVP is instead related to second boiling then the $H_2O/CO_2$ ratio of the residual melt would necessarily be high and would promote coalescence versus nucleation[73]. The exsolution of MVP could also be triggered by the incipient crystallization of ilmenite in the late residual melt with related progressive exsolution of the MVP at the developing crystal-melt interface with entrapment of FI.

## Conclusions

We document here the presence of inferred primary FI in ilmenite which are suggested to represent the trapping of the MVP generated in the latter stages of magma crystallization in two different basic igneous settings. Although the evidence for volatile saturation and magmatic FI in basic magmas is previously reported in other similar settings, the occurrence of primary FI in ilmenite is here recognized and studied for the first time to the best of our knowledge. This study thus highlights that ilmenite might be a suitable host for the MVP, especially where it has not experienced important sub-solidus modification which, as noted herein, can easily be recognized due to the presence of secondary reaction products (e.g., titanite ± rutile).

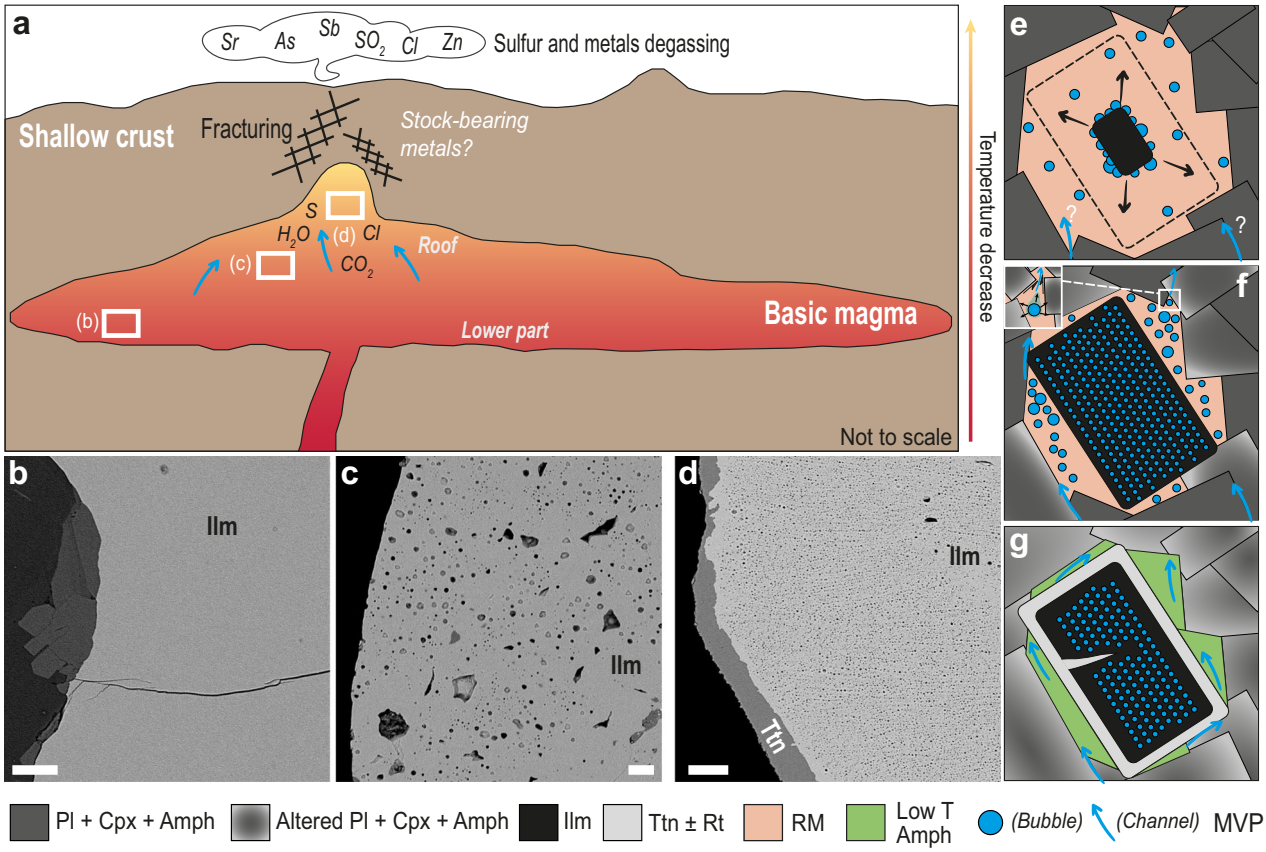


**Fig. 7 | Schematic diagram illustrating the conceptual model of entrapment of magmatic volatile phases within ilmenite. a** General geometry (not to scale) of a gabbroic intrusion with the location of insets (**b**), (**c**) and (**d**). **b–d** Back-scattered electron (BSE) images of ilmenite (Ilm) texture from the lower (**b**), central (**c**) and upper (**d**) parts of the basic intrusion that records magma degassing from the base to the top. White scale bar represents 20 µm. **e** Onset of volatile exsolution in the residual melt (RM) of the mush and release of a magmatic volatile phase (MVP) via second boiling. Ilmenite may act as a preferential site for nucleation of bubbles during its growth or incipient ilmenite crystallization may act as the trigger of progressive exsolution of bubbles at the developing crystal-melt interface. **f** Ilmenite grain crystallizes more or less quickly and may easily traps abundant MVP as fluid inclusions (FI) during its progressive crystallization and magma cooling. **g** Following ilmenite formation, trapped FI likely undergo re-equilibration via necking, whereas the untrapped MVP likely escapes via capillary fracturing or others processes and probably coalesce towards the surface. The latter MVP interacts with and modifies earlier crystallized silicate phases. Interaction of ilmenite with fluids saturated in Si and Ca (due to alteration of calcic plagioclase (Pl) and mafic minerals) causes ilmenite breakdown. This fracture-controlled subsolidus alteration is responsible for the formation of FI-free ilmenite and the development of secondary titanite (Ttn) ± rutile (Rt). Cpx - clinopyroxene, Amph - amphibole, Low T - low temperature.

As the noted FI reported record the late-stage volatile saturation in basic magmas, it offers the rare opportunity to study the chemistry and metal enrichment of such magmatic fluids produced in highly crystallized basic magmas. Although qualitative at this time, our results showed that the FI chemistry (i.e., Na-Ca-Cl-S-Fe for solute composition and Cu, Sn, Mo, Sb, W, and Pb for metal and metalloids) is consistent with what is known and expected for magmatic fluids associated with basic magmas. Additional studies are, however, needed to further quantify the composition (especially solvent species such as $H_2O$ or $CO_2$ for instance) and enhance the understanding of volatile saturation in basic magmas, as it was not the focus of this study. In this regard, future work might involve the use of high-resolution nano-computed tomography (nanoCT) to quantify the 3D distribution of FI[74], whereas focused ion beam-scanning electron microscope (FIB-SEM)[75,76] and/or time-of-flight secondary ion mass spectrometry (TOF-SIMS)[77] could help to quantify the presence of daughter minerals (without contamination due to polishing), volatile species such as $H_2O$, $CO_2$, sulfur species, and chlorine–bearing compounds, as well as metals.

Finally, this study should encourage others to apply similar methods to look for FI in ilmenite and other opaque phases for those interested in better documenting the presence and nature of the MVP during the latter stages of magma crystallization, which is otherwise challenging to do. This consideration is particularly relevant for contentious settings, where the presence and origin of the fluid phase are still debated. Hence, the implication might be far reaching for both igneous petrology and relevant ore-forming environments in basic-to-mafic systems.

## Methods

For this study, we investigated six representative rock samples from the lower, central, and upper parts of the SJD intrusion and two samples from the roof zone of the CS basic sills (Supplementary Fig. 1 & Supplementary Table 1). A comprehensive suite of analytical techniques was used to study the materials and document the presence, distribution, nature and qualitative chemistry of the FI in ilmenite. Ilmenite was studied on thin and thick sections, as well as polished epoxy mounts in which ilmenite was previously separated and handpicked. About 400 ilmenite grains were characterized using reflected light (RL) microscopy and scanning electron microscopy (SEM) coupled to an energy dispersive spectrometer (EDS). Some ilmenite grains were further analyzed with electron backscatter diffraction (EBSD) and electron micro-probe analyzer (EPMA), the latter providing high-resolution elemental maps. Thick sections of the material were heated to induce decrepitation of FI and formation of evaporate (i.e., salt) mounds which were subsequently analyzed using SEM-EDS to quantify their chemistry with a few selected for elemental mapping with the EPMA. Laser ablation inductively coupled mass spectrometry (LA ICP-MS) was used to qualitatively characterize the chemistry of ilmenite and also to determine the minor- and trace-element chemistry of evaporate mounds. Note that we

prepared double polished thick sections for infrared micro-thermometric FI studies analyses, but the opaqueness of ilmenite and small size of FI precluded observing any FI. We also tried to quantify the 3D distribution of FI by using a Nanotom 180 NF Phoenix X-Ray micro-computed tomography, but the resolution (i.e., 1.2 µm) was not high enough for imaging FI, as most of them being lower than 2 µm.

### Quantitative chemical analyses by EPMA

Quantitative analyzes of ilmenite from CS were acquired using a Cameca SX-Five EPMA at the common laboratory of the Earth Sciences Institute of Orléans (ISTO) and the French Geological Survey (BRGM) laboratory (Orléans, France). Analyzes were performed at an accelerating voltage of 15 kV, a beam current of 10 nA, and with a focused beam, using the following mineral standards: albite (SiKα), hematite (FeKα), MgO (MgKα), and pyrophanite (TiKα, MnKα). Analyzed elements, detailed lists, and detection limits can be found in Supplementary Table 2. Mineral formula stoichiometric charge balanced mineral recalculations were used to determine the amount of $Fe^{3+}$ present in ilmenite[78]. X-ray elemental maps of ilmenite crystals were acquired with the IHP 200 F JEOL EPMA of the ISTO laboratory, using the following operating conditions: 20 kV, 40 nA, 100 ms dwell time and 0.26 µm step.

### Electron backscatter diffraction

Scanning electron microscopy (SEM) and electron backscatter diffraction (EBSD) analyzes were performed on thick and thin sections, both polished at ISTO-BRGM (Orléans, France) using diamond pastes with decreasing granulometries from 3 to 0.25 µm followed by chemico-mechanical polishing using colloidal silica. Each sample was carbon coated (i.e., around 3 nm) to prevent electron charging during EBSD acquisition. The backscattered electron (BSE) images were acquired using a Gemini I field Emission Gun from Zeiss and a TESCANx MIRA 3 XMU equipped with an EDAX Pegasus system available at the ISTO-BRGM. The latter was also used to acquire the EBSD data. While SEM observations were acquired at an accelerating voltage of 15 kV and a beam current of 2–3 nA, EBSD acquisition were performed at 30 kV and 5–6 nA at a working distance of 15 mm. EBSD acquisitions were performed on thin sections tilted at 70°. Data acquisition and post-analyzing cleaning were performed using the TSL-OIM software (OIM data collection and OIM analysis version 7.1; https://www.edax.com/products/ebsd/oim-analysis) and a map cleaning procedure[79]. A step size of 1 µm was used for each map. The data were subsequently treated and plotted using the open-source MTEX toolbox (version 5.10; https://mtex-toolbox.github.io) for MATLAB. The minimum angles of lattice misorientation to define grain and intragranular boundaries were respectively set to 10° and 2°, each grain containing a minimum of five consecutive pixels on several rows. While continuous low-angle boundaries are referred to as sub-grain boundaries, the discontinuous ones are referred to as inner boundaries. For indexing, we used a trigonal symmetry (point group −3) to avoid artefacts related to twinning in ilmenite.

### Laser ablation inductively coupled plasma mass spectrometry

Trace element concentrations of ilmenite were determined in situ by LA ICP-MS at ISTO. The system consists of a RESOlution-SE (ASI) 193 nm excimer laser with an S155 ablation cell (Laurin Technic) coupled to an Agilent 8900 triple inductively coupled plasma quadrupole mass spectrometer (QQQ-ICP-MS). Ablation was carried out using a He carrier gas which was mixed with Ar as a cell and nebulizer gas. Calibration was performed before each analytical session on NIST SRM 612 reference glass minimizing U/Th fractionation ( ~ 0.998 %), and the production of oxides ($ThO^+/Th^+$ ~ 0.128 %) and doubly-charged ions ($Ca^{2+}/Ca^+$ ~ 0.289). A laser beam size of 20 µm, a repetition rate of 10 Hz and a fluence of 3 J/cm$^2$ were used. Single analysis consists of 30 s of background collection followed by 40 s of ablation and 15 s of wash-out delay. For each analytical session, about 2–5 reference materials were analyzed before and after each set of 12–15 sample analyses, following classical bracketing procedure. The Ti content of the ilmenite, as determined from electron probe microanalysis, was used as the internal standard to quantify trace element concentrations. GSE-2g was the primary reference material, and NIST610 and BCR-2g glasses used as quality control materials. Data reduction was carried out using the commercial data reduction software GLITTER[80]. Traverse profiles of ilmenite were acquired with a laser beam of 30 µm, a repetition rate of 7 Hz, a fluence of 3 J/cm$^2$ and a scanning speed of 20 µm/s.

### Evaporate mound coupled with SEM-EDS, EPMA and LA ICP-MS analyses

The solute chemistry of FI was determined using the evaporate mound method[42,81,82] in order to define the qualitative composition of trapped FI in ilmenite from five samples from SJD and four from CS. The thick sections were heated at a rate of 50 °C / min to about 600 °C to induce decrepitation of the contained FI and subsequently carbon-coated for SEM-EDS analysis and X-ray elemental maps. The maps were acquired with a Cameca SX-Five EPMA at the ISTO-BRGM laboratory, using the following operating conditions: 22 kV, 100 nA, 100 ms dwell time and 0.5 µm step.

LA ICP-MS traverses, using the aforementioned ISTO instrument, were performed on decrepitate mounds coating the surfaces of ilmenite for estimating some of the trace elements and thus the solute chemistry of the FI. The laser was operated at a repetition rate of 10 Hz and fluence of 3 J/cm2 on the sample surface. Traverse profiles were acquired with a laser beam of 10 µm and a scanning speed of 5 µm/s. The raw data were processed by Iolite 2.5 software[83] using the trace element data reduction scheme[84]. The latter results were converted into time-slice data whereby each complete sweep of the mass spectrometer (e.g., about 0.5 s) is considered equivalent to a conventional point analysis[85]. No internal standard was used, and consequently the data are qualitative.

## Data availability

The LA ICP-MS data used for the Fig. 4 in this manuscript are published on figshare (https://doi.org/10.6084/m9.figshare.27045316.v2). All remaining data used in this paper are included in the main article and its supplementary information file.

Received: 17 May 2024; Accepted: 14 October 2024;
Published online: 25 October 2024

## References

1. Sorby, H. C. On the microscopical structure of crystals indicating the origin of rocks and minerals. *Quart. J. Geol. Soc. Lond.* **14**, 453–500 (1858).
2. Blamey, N. J. F. & Brand, U. Atmospheric gas in modern and ancient halite fluid inclusions: A screening protocol. *Gondwana Res.* **69**, 163–176 (2019).
3. Lowenstein, T. K., Timofeeff, M. N., Brennan, S. T., Hardie, L. A. & Demicco, R. V. Oscillations in phanerozoic seawater chemistry: evidence from fluid inclusions. *Science* **294**, 1086–1088 (2001).
4. Goldstein, R. H. Fluid inclusions in sedimentary and diagenetic systems. *Lithos* **55**, 159–193 (2001).
5. Bodnar, R. J., Lecumberri-Sanchez, P., Moncada, D. & Steele-MacInnis, M. Fluid inclusions in hydrothermal ore deposits, *in Treatise on Geochemistry* (second edition), **Vol. 13**: Geochemistry of Mineral Deposits: Oxford, UK (ed. Scott, S. D.) 119–142 (Elsevier, 2014).
6. Touret, J. L. R. & Huizenga, J. M. Fluid-assisted granulite metamorphism: A continental journey. *Gondwana Res.* **21**, 224–235 (2012).
7. Carvalho, B. B. et al. Primary $CO_2$-bearing fluid inclusions in granulitic garnet usually do not survive. *Earth Planet Sc. Lett.* **536**, 116170 (2020).
8. Andersen, T. & Neumann, E. R. Fluid inclusions in mantle xenoliths. *Lithos* **55**, 301–320 (2001).
9. Campbell, A. R., Hackbarth, C. J., Plumlee, G. S. & Petersen, U. Internal features of ore minerals seen with the infrared microscope. *Econ. Geol.* **79**, 1387–1392 (1984).

10. Lüders, V. Contribution of infrared microscopy to studies of fluid inclusions hosted in some opaque ore minerals: possibilities, limitations, and perspectives. *Miner. Depos.* **52**, 663–673 (2017).
11. Cashman, K. V. Volatile controls on magma ascent and eruption. *Geophys. Monogr. Ser.* **150**, 109–124 (2004).
12. Audétat, A., Pettke, T., Heinrich, C. A. & Bodnar, R. J. The composition of magmatic hydrothermal fluids in barren versus mineralized intrusions. *Econ. Geol.* **103**, 877–908 (2008).
13. Blundy, J., Mavrogenes, J., Tattitch, B., Sparks, S. & Gilmer, A. Generation of porphyry copper deposits by gas–brine reaction in volcanic arcs. *Nat. Geosci.* **8**, 235–240 (2015).
14. Barnes, S. J. et al. Role of volatiles in intrusion emplacement and sulfide deposition in the supergiant Norilsk-Talnakh Ni-Cu-PGE ore deposits. *Geology* **51**, 1027–1032 (2023).
15. Hedenquist, J. W. & Lowenstern, J. B. The role of magmas in the formation of hydrothermal ore deposits. *Nature* **370**, 519–527 (1994).
16. Mungall, J. & Naldrett, A. N. Ore deposits of the Platinum-group elements. *Elements* **4**, 253–258 (2008).
17. Iacono-Marziano, G. et al. 2022, The critical role of magma degassing in sulphide melt mobility and metal enrichment. *Nat. Commun.* **13**, 1–10 (2022).
18. Wallace, P. J. Volatiles in subduction zone magmas: concentrations and fluxes based on melt inclusion and volcanic gas data. *J. Volcanol. Geotherm. Res.* **140**, 217–240 (2005).
19. Kent, A. J. R. Melt inclusions in basaltic and related volcanic rocks. *Rev. Mineral. Geochem.* **69**, 273–331 (2008).
20. Métrich, N. & Wallace, P. J. Volatile abundances in basaltic magmas and their degassing paths tracked by melt inclusions. *Rev. Mineral. Geochem.* **69**, 363–402 (2008).
21. Edmonds, M. & Woods, A. W. Exsolved volatiles in magma reservoirs. *J. Volcanol. Geotherm. Res.* **368**, 13–30 (2018).
22. Kelley, D. S., Gillis, K. M. & Thompson, G. Fluid evolution in submarine magma-hydrothermal systems at the Mid-Atlantic Ridge. *J. Geophys. Res. Solid Earth* **98**, 19579–19596 (1993).
23. Kelley, D. S. & Malpas, J. Melt-fluid evolution in gabbroic rocks from Hess Deep. *Proc. Integr. Ocean Drill. Program, Sci. Results* **147**, 213–226 (1996).
24. Kelley, D. S. & Früh-Green, G. L. Volatile lines of descent in submarine plutonic environments: insights from stable isotope and fluid inclusion analyses. *Geochim. Cosmochim. Acta* **65**, 3325–3346 (2001).
25. Hennings, S. K., Wagner, T., Ulmer, P. & Heinrich, C. A. Fluid evolution of the monte mattoni mafic complex, adamello batholith, Northern Italy: insights from fluid inclusion analysis and thermodynamic modeling. *J. Petrol.* **58**, 1645–1670 (2017).
26. Dixon, J. E. & Stolper, E. M. An experimental study of water and carbon dioxide solubilities in mid-ocean ridge basaltic liquids. Part II: applications to degassing. *J. Petrol.* **36**, 1633–1646 (1995).
27. Kelley, D. S., Robinson, P. T. & Malpas, J. G. Processes of brine generation and circulation in the oceanic crust: Fluid inclusion evidence from the Troodos Ophiolite, Cyprus. *J. Geophys. Res. Solid Earth* **97**, 9307–9322 (1992).
28. Bodnar, R. J., Burnham, C. W. & Sterner, S. M. Synthetic fluid inclusions in natural quartz. III. Determination of phase equilibrium properties in the system $H_2O$-NaCl to 1000 °C and 1500 bars. *Geochim. Cosmochim. Acta* **49**, 1861–1873 (1985).
29. Fournier, R. O. Conceptual models of brine evolution in magmatic-hydrothermal systems. *USG S Prof. Pap.* **1350**, 1487–1505 (1987).
30. Kelley, D. S. & Delaney, J. R. Two-phase separation and fracturing in mid-ocean ridge gabbros at temperatures greater than 700 °C. *Earth Planet. Sc. Lett.* **83**, 53–66 (1987).
31. Castelain, T., McCaig, A. M. & Cliff, R. A. Fluid evolution in an Oceanic Core Complex: A fluid inclusion study from IODP hole U1309 D—Atlantis Massif, 30°N, Mid-Atlantic Ridge. *Geochem. Geophys. Geosyst.* **15**, 1193–1214 (2014).
32. Cline, J. S. & Bodnar, R. J. Can economic porphyry copper mineralization be generated by a typical calc-alkaline melt? *J. Geophys. Res. Solid Earth* **96**, 8113–8126 (1991).
33. Bodnar, R. J. Synthetic fluid inclusions: XII. The system $H_2O$-NaCl. Experimental determination of the halite liquidus and isochores for a 40 wt% NaCl solution. *Geochim. Cosmochim. Acta* **58**, 1053–1063 (1994).
34. Barboni, M. et al. Timing of incremental pluton construction and magmatic activity in a back-arc setting revealed by ID-TIMS U/Pb and Hf isotopes on complex zircon grains. *Chem. Geol.* **342**, 76–93 (2013).
35. Caroff, M. et al. The mafic-silicic layered intrusions of Saint-Jean-du-Doigt (France) and North-Guernsey (Channel Islands), Armorican Massif: Gabbro-diorite layering and mafic cumulate pegmatoid association. *Lithos* **125**, 675–692 (2011).
36. Pochon, A., Iacono-Marziano, G., Gloaguen, E., Tuduri, J. & Erdmann, S. High-temperature alteration during cooling of mafic intrusions: Insights from the Saint-Jean-du-Doigt intrusive complex (Armorican Massif, France). *Lithos* **436-437**, 106977 (2023).
37. Campos Rodríguez, et al. Mafic magmatism in the Central Iberian Zone: Towards a better understanding of Sb mineralization? In 17th *SGA Biennial Meeting, Zürich, Extended Abstracts*, 8–11 (2023).
38. López-Moro, F. J., Murciego, A. & López-Plaza, M. Silurian/Ordovician asymmetrical sill-like bodies from La Codosera syncline, W Spain: A case of tholeiitic partial melts emplaced in a single magma pulse and derived from a metasomatized mantle source. *Lithos* **96**, 567–590 (2007).
39. López-Moro, F. J., Murciego, A., López-Plaza, M., Romer, R. L. & de Rafélis, M. 2020, Sequential crystal overproduction triggering Mg-Cr-Ti-V-P-MREE- enrichment in a single-pulse tholeiitic mafic sill in the Central Iberian Zone, Spain. *Lithos* **362-363**, 105464 (2020).
40. Roedder, E. Fluid Inclusions. in *Reviews in Mineralogy* **12** (Mineralogical Society of America, 1984).
41. Bodnar, R. J. Reequilibration of fluid inclusions. in *Fluid Inclusions: Analysis and Interpretation*, Short Course **32** (eds. Samson, I., Anderson, A. & Marshall, D.) (Mineralogical Association of Canada, 2003).
42. Kontak, D. J. Analysis of evaporate mounds as a complement to fluid inclusion thermometric data: Case studies from granitic environments in Nova Scotia and Peru. *Canad. Mineral.* **42**, 1315–1329 (2004).
43. Klemme, S., Günther, D., Hametner, K., Prowatke, S. & Zack, T. The partitioning of trace elements between ilmenite, ulvospinel, armalcolite and silicate melts with implications for the early differentiation of the moon. *Chem. Geol.* **234**, 251–263 (2006).
44. Shepherd, K., Namur, O., Toplis, M. J., Devidal, J. L. & Charlier, B. Trace element partitioning between clinopyroxene, magnetite, ilmenite and ferrobasaltic to dacitic magmas: an experimental study on the role of oxygen fugacity and melt composition. *Contrib. Mineral. Petrol.* **177**, 1–21 (2022).
45. Candela, P. A. & Bouton, S. L. The influence of oxygen fugacity on tungsten and molybdenum partitioning between silicate melts and ilmenite. *Econ. Geol.* **85**, 633–640 (1990).
46. Wei, C., Xiong, X., Wang, J., Huang, F. & Gao, M. Partitioning of tin between mafic minerals, Fe-Ti oxides and silicate melts: Implications for tin enrichment in magmatic processes. *Geochim. Cosmochim. Acta* **372**, 81–100 (2024).
47. Putnis, A. Mineral Replacement Reactions. *Rev. Mineral. Geochem.* **70**, 87–124 (2009).
48. Angiboust, S. & Harlov, D. Ilmenite breakdown and rutile-titanite stability in metagranitoids: Natural observations and experimental results. *Am. Mineral.* **102**, 1696–1708 (2017).
49. Pochon, A. et al. Metal mobility during hydrothermal breakdown of Fe-Ti oxides: Insights from Sb-Au mineralizing event (Variscan Armorican Massif, France). *Ore Geol. Rev.* **91**, 66–99 (2017).
50. Putnis, A. Fluid–mineral interactions: controlling coupled mechanisms of reaction, mass transfer and deformation. *J. Petrol.* **62**, egab092 (2021).

51. Burnham, C. W. Magmas and hydrothermal fluids. *Geochem. Hydrothermal Ore Depos.* **71**, 136 (1979). ed. Barnes, H. L.
52. Bodnar, R. J. & Student, J. J. Melt inclusions in plutonic rocks: Petrography and microthermometry. in *Melt Inclusions in Plutonic Rocks*, Short Course **36** (ed. Webster, J. D.) 1–26 (Mineralogical Association of Canada, 2006).
53. Veksler, I. V. Crystallized melt inclusions in gabbroic rocks. in *Melt Inclusions in Plutonic Rocks*, Short Course **36**, (ed. Webster, J.D.) 1–26 (Mineralogical Association of Canada, 2006).
54. Candela, P. A. A review of shallow, ore-related granites: Textures, volatiles, and ore metals. *J. Petrol.* **38**, 1619–1633 (1997).
55. London, D. Pegmatites. (Mineralogical Association of Canada, 2008).
56. Zajacz, Z., Candela, P. A., Piccoli, P. M. & Sanchez-Valle, C. The partitioning of sulfur and chlorine between andesite melts and magmatic volatiles and the exchange coefficients of major cations. *Geochim. Cosmochim. Acta* **89**, 81–101 (2012).
57. Edmonds, M., Mason, E. & Hogg, O. Volcanic outgassing of volatile trace metals. *Ann. Rev. Earth Planet. Sci.* **50**, 79–98 (2022).
58. Behrens, H. & Gaillard, F. Geochemical aspects of melts: volatiles and redox behavior. *Elements* **2**, 275–280 (2006).
59. Iacono-Marziano, G., Morizet, Y., Le Trong, E. & Gaillard, F. New experimental data and semi-empirical parameterization of $H_2O$–$CO_2$ solubility in mafic melts. *Geochim. Cosmochim. Acta* **97**, 1–23 (2012).
60. Spear, F. S. & Selverstone, J. Water exsolution from quartz: Implications for the generation of retrograde metamorphic fluids. *Geology* **11**, 82–85 (1983).
61. Philippot, P., Chevallier, P., Chopin, C. & Dubessy, J. Fluid composition and evolution in coesite-bearing rocks (Dora-Maira massif, Western Alps): implications for element recycling during subduction. *Contrib. Mineral. Petrol.* **121**, 29–44 (1995).
62. Zhang, Z., Shen, K., Liou, J. G. & Zhao, X. Fluid inclusions associated with exsolved quartz needles in omphacite of UHP eclogites, chinese continental scientific drilling main drill hole. *Int. Geol. Rev.* **49**, 479–486 (2007).
63. Johnson, E. A. Water in Nominally Anhydrous Crustal Minerals: Speciation, Concentration, and Geologic Significance. *Rev. Mineral. Geochem.* **62**, 117–154 (2006).
64. Jiang, S.-Y. & Palmer, M. R. Mn-rich ilmenite from the Sullivan Pb-Zn-Ag deposit. *Br. Columbia Canad. Mineral.* **34**, 29–36 (1996).
65. Essaifi, A., Ballèvre, M., Marignac, C. & Capdevila, R. Découverte et signification d'une paragenèse à ilménite zincifère dans les métapélites des Jebilet centrales (Maroc). *C. R. Acad. Sci.* **333**, 381–388 (2001).
66. Parmigiani, A., Degruyter, W., Leclaire, S., Huber, C. & Bachmann, O. The mechanics of shallow magma reservoir outgassing. *Geochem. Geophys. Geosyst.* **18**, 2887–2905 (2017).
67. Trosh, J., Huber, C. & Bachmann, O. The physical and chemical evolution of magmatic fluids in near-solidus silicic magma reservoirs: Implications for the formation of pegmatites. *Am. Mineral.* **107**, 190–205 (2022).
68. Hurwitz, S. & Navon, O. Bubble nucleation in rhyolitic melts: experiments at high pressure, temperature and water content. *Earth Planet. Sci. Lett.* **122**, 267–280 (1994).
69. Edmonds, M., Brett, A., Herd, R. A., Humphreys, M. C. S. & Woods, A. Magnetite-bubble aggregates at mixing interfaces in andesite magma bodies. *Geol. Soc. Spec. Publ.* **410**, 95–121 (2015).
70. Gardner, J. E. et al. Bubble formation in magma. *Ann. Rev. Earth Planet. Sci.* **51**, 131–154 (2023).
71. Navon, O. & Lyakhovsky, V. Vesiculation processes in silicic magmas. *Geol. Soc. Spec. Publ.* **145**, 27–50 (1998).
72. Cáceres, F. et al. Can nanolites enhance eruption explosivity? *Geology* **48**, 997–1001 (2020).
73. Buono, G. et al. Dynamics of degassing in evolved alkaline magmas: Petrological, experimental and theoretical insights. *Earth-Sci. Rev.* **211**, 103402 (2020).
74. Richard, A. et al. Advances in 3D imaging and volumetric reconstruction of fluid and melt inclusions by high resolution X-ray computed tomography. *Chem. Geol.* **508**, 3–14 (2019).
75. Anderson, A. & McCarron, T. Three-dimensional textural and chemical characterization of polyphase inclusions in spodumene using a dual focused ion beam - scanning electron microscope (FIB-SEM). *Canad. Mineral.* **49**, 541–553 (2011).
76. Berkesi, M. et al. The role of $CO_2$-rich fluids in trace element transport and metasomatism in the lithospheric mantle beneath the Central Pannonian Basin, Hungary, based on fluid inclusions in mantle xenoliths. *Earth Planet. Sc. Lett*. **331–332**, 8–20 (2012).
77. Nakamura, T. et al. Formation and evolution of carbonaceous asteroid Ryugu: Direct evidence from returned samples. *Science* **379**, eabn8671 (2023).
78. Droop, G. T. R. A general equation for estimating $Fe^{3+}$ concentrations in ferromagnesian silicates and oxides from microprobe analyses, using stoichiometric criteria. *Mineral. Mag.* **51**, 431–435 (1987).
79. Précigout, J., Prigent, C., Palasse, L. & Pochon, A. Water pumping in mantle shear zones. *Nat. Commun.* **8**, 1–10 (2017).
80. Griffin, W. L. GLITTER: data reduction software for laser ablation ICP-MS. *Laser Ablation ICP-MS in the Earth Sciences: Current practices and outstanding issues*, 308–311 (2008).
81. Haynes, F. M. & Kesler, S. E. Chemical evolution of brines during Mississippi Valley-type mineralization: evidence from East Tennessee and Pine Point. *Econ. Geol.* **82**, 53–71 (1987).
82. Haynes, F. M., Sterner, S. M. & Bodnar, R. J. Synthetic fluid inclusions in natural quartz. IV. Chemical analyses of fluid inclusions by SEM/EDA: evaluation of method. *Geochim. Cosmochim. Acta* **52**, 969–977 (1988).
83. Paton, C., Hellstrom, J., Paul, B., Woodhead, J. & Hergt, J. Iolite: Freeware for the visualisation and processing of mass spectrometric data. *J. Anal. Spectrom.* **26**, 2508–2518 (2011).
84. Woodhead, J. D., Hellstrom, J., Hergt, J. M., Greig, A. & Maas, R. 2007, Isotopic and elemental imaging of geological materials by laser ablation inductively coupled plasma-mass spectrometry. *Geostand. Geoanal. Res.* **31**, 331–343 (2007).
85. Gourcerol, B., Kontak, D. J., Thurston, P. C. & Petrus, J. A. Application of LA-ICP-MS sulfide analysis and methodology for deciphering elemental paragenesis and associations in addition to multi-stage processes in metamorphic gold settings. *Canad. Mineral.* **56**, 39–64 (2018).
86. Buddington, A. F. & Lindsley, D. H. Iron–titanium oxide minerals and synthetic equivalents. *J. Petrol.* **5**, 310–357 (1964).


## Acknowledgements

This article is dedicated to the memory and scientific legacy of Dr. Eric Gloaguen, who passed away prematurely. This work was carried out in the framework of the ERA-MIN2 Aureole project (i.e., tArgeting eU cRitical mEtals (Sb, W) and predictibility of Sb-As-Hg envirOnmentaL issuEs) with funding from the ANR (grant ANR-19-MIN2-0002) for the French partners. The LabEx VOLTAIRE (ANR-10-LABX-100-01) and EquipEx PLANEX (ANR-11-EQPX-0036) are also acknowledged to have provided support for the electron microprobe and LA-ICP-MS laboratories. All the samples used in this study did not require permissions, except sample coming from the quarry belonging to Villar del Rey Natural Stones S.L., where we had permissions from company. The authors thank Ida Di Carlo, Guillaume Wille and Saskia Erdmann for their help with the EPMA, EBSD and LA ICP-MS analyses, respectively. This project has benefited from the expertise and the facilities of the Platform MACLE - CVL which was co-funded by the European Union and Centre-Val de Loire Region (FEDER). D. Kontak acknowledges financial support from ANR - Carnot (N° 19-CARN-003-01, convention N° 16-CARN-003-01) which facilitated this research. The authors sincerely acknowledge the insightful reviews provided by R. J. Bodnar, D. Moncada, and Z. Zajacz which resulted in a much improved manuscript and clarification of several important points.

## Author contributions

A.P., E.G. & G.I-M. have designed the research and A.P. & D.J.K wrote the original draft. A.P., D.J.K., G.I-M., E.G., J.T. & H.C.R. carried out field investigations and sampling. A.P., G.I-M. and T.C. performed SEM-EDS, EPMA and LA ICP-MS analyses. J.P. provided support for EBSD analysis and interpretation. D.J.K., G.I-M., E.G., J.T., T.C., J.P., V.M., B.G. and L.M. contributed to discussions, editing, and revisions.

## Competing interests

The authors declare no competing interests.

## Additional information

**Supplementary information** The online version contains supplementary material available at https://doi.org/10.1038/s43247-024-01788-8.

**Correspondence** and requests for materials should be addressed to Anthony Pochon.

**Peer review information** *Communications Earth & Environment* thanks Daniel Moncada, Zoltan Zajacz and Robert J Bodnar for their contribution to the peer review of this work. Primary Handling Editor: Carolina Ortiz Guerrero. A peer review file is available